



ARTICLE

Remarkably Enhanced Photodegradation of Organic Pollutants by NH₂-UiO-66/ZnO Composite under Visible-Light Irradiation

Dehong Teng^{1,#}, Jing Zhang^{1,#}, Xinzhi Luo¹, Fei Jing¹, Hengwei Wang¹, Jing Chen^{1,*}, Chao Yang¹, Shaohong Zang^{1,*} and Yingtang Zhou^{1,2}

¹National Engineering Research Center for Marine Aquaculture, Zhejiang Ocean University, Zhoushan, 316004, China

²Marine Science and Technology College, Zhejiang Ocean University, Zhoushan, 316004, China

*Corresponding Authors: Jing Chen. Email: z20095136216@zjou.edu.cn; Shaohong Zang. Email: shzang@zjou.edu.cn

#These authors contributed equally to this work

Received: 09 September 2021 Accepted: 24 November 2021

ABSTRACT

Semiconductor photocatalysis is a novel highly efficient and low-cost method for removing organic pollutants from wastewater. However, the photoreduction performance of semiconductors on organic pollutants is limited due to the weak absorption of visible light caused by its wide band gap and low carrier utilization rate resulting from severe electron-holes recombination. In the present study, flower-like NH₂-UiO-66 (NU66)/ZnO nanocomposites were prepared using a facile method and exhibited high efficiency under visible light driven photocatalysts. The X-ray diffractometer (XRD), scanning electron microscope (SEM), transmitter electron microscope (TEM), and X-ray photoelectron spectroscopy (XPS) were used to characterize the prepared samples, indicating that NU66/ZnO was successfully synthesized. The photocatalytic activity of the prepared NU66/ZnO nanocomposites was determined by measuring the photodegradation of methylene blue (MB) and malachite green (MG) under visible-light irradiation. The optimal nanocomposite loading of 5% wt NU66 to NU66/ZnO demonstrated the highest photocatalytic activity for the degradation of MB. The photocatalytic activity of a 5% NU66/ZnO composite was approximately 95-fold and 19-fold higher than that of NU66 and ZnO samples, respectively. The enhanced activity of the 5% wt NU66/ZnO nanocomposite was further confirmed through photoelectrochemical analysis. The formation of type II heterojunctions between the counterparts significantly suppressed recombination of the photogenerated charge carriers. Photocatalytic degradation experiments with different quenchers indicated that the effect of superoxide anion radicals ($\cdot\text{O}_2^-$) had a greater effect than the other scavengers. Additionally, the improved photocatalytic mechanism underlying the activity of NU66/ZnO nanocomposites was also explored. These findings establish a basis for development of MOF based heterojunction for photocatalytic organic pollution remediation.

KEYWORDS

Photodegradation; heterojunction; MOF; NH₂-UiO-66; ZnO

1 Introduction

In recent decades, population growth and the industrialization process have increased the demand for organic dyes [1]. Organic dyes are mainly used in textile industries, ink production, chemical analysis,



This work is licensed under a Creative Commons Attribution 4.0 International License, which permits unrestricted use, distribution, and reproduction in any medium, provided the original work is properly cited.

and ceramic industries resulting in the release of pollutants into waste water [2,3]. Organic dyes have a variety of biological effects, including toxicity and carcinogenicity, posing a major threat to ecological balance [4]. As a result, it is critical to find efficient ways for degrading organic dyes.

Current methods used for the elimination and degradation of organic dyes include adsorption, physical/chemical precipitation, biological methods, and photo-degradation [5]. These traditional methods, however, are incapable of removing organic pollutants from the roots. Semiconductor photocatalytic technology can be used to circumvent the limitations of conventional methods. Photocatalytic degradation of organic pollutants in water is a novel wastewater treatment technology, and several studies have verified its efficacy in wastewater treatment. Photocatalytic technology can directly utilize sunlight to achieve significant degradation of organic pollutants [6]. This novel technique exhibits the advantages of strong oxidizing ability and low cost. Therefore, photocatalytic degradation methods are recommended as environmentally friendly, cheap, and efficient [7,8]. Although the photocatalytic method is cost-effective, it has low photocatalytic efficiency. In addition, low efficiency caused by recombination of photo-generated electron-hole pairs and the high cost of photocatalysts limits the industrial application of solar-driven degradation. Moreover, it is also hampered by the low recyclability of the photocatalyst powder [9,10]. Therefore, it is imperative to explore green, cheap and efficient materials for photodegradation.

Several popular materials such as TiO₂, ZnO, MoS₂, PCN, and CNT have been explored as photocatalysts for photodegradation [11–13]. Among them, ZnO is extensively used as a photocatalyst owing to its safety, cheap, facile synthesis, and high stability [14]. ZnO can degrade organic dye pollutants into non-toxic and harmless substances (CO₂ and H₂O) under visible-light-driven photocatalysts. However, low solar energy utilization and a high risk of recombination charge carriers limit the photocatalytic degradation efficiency of ZnO. Therefore, ZnO must improve broad solar energy and reduce the recombination charge carriers modified with co-catalysts (Au, Pt, Ag, Ce, etc.) to establish heterojunctions such as CuO/ZnO, ZnS/ZnO, and RGO/ZnO [15,16], which is a universal strategy for improving photocatalysis performance [17–19].

Metal-organic frameworks (MOFs) have attracted significant attention for their potential as high-profile photocatalysts owing to their ability to develop a wide range of structures with high diversity [20]. The unique properties of MOFs can be attributed to their inorganic-organic hybrid compositions, in which the inorganic metal nodes can act as charge transmitters and the organic ligands are effective in harvesting solar light [21]. A recent study developed a Zr-MOF referred to as NH₂-UiO-66 (NU66) with high stability [22]. Du et al. [23] fabricated NU66 as a photocatalyst for selective oxidation of alcohol and aqueous Cr reduction (VI). Zhang et al. [24] also designed an Ag/AgCl/NH₂-UiO-66 hybridized heterojunction, which exhibited improved photodegradation efficiency. In addition, Zhao et al. [25,26] synthesized NH₂-UiO-66/ZnIn₂S₄ (NU66/ZIS) composites and demonstrated increased charge transfer and separation efficiency. It further expands the NU66 application [27].

In the present study, a series of NU66/ZnO heterojunctions were developed using a facile hydrothermal method for photodegradation of MB and MG under irradiation with visible light. The composite exhibited high visible light absorption, more active sites, and a faster charge transfer rate. The optimized photodegradable activity of MB by NU66/ZnO was approximately 95-fold and 19-fold higher than NU66 and ZnO, respectively. EPR analysis showed that the superoxide anion radicals ($\bullet\text{O}_2^-$) were the active species in the NU66/ZnO combination. The possible reaction mechanism of photodegradation of NU66/ZnO was investigated using UV-Vis DRS, PL/TRPL, and photoelectrochemical analyses.

2 Materials and Methods

2.1 Characterization of the Samples and Reagents

The synthetic raw materials of the sample come from Sinopharm Chemical Reagent, including Zinc acetate dihydrate ($\geq 99.0\%$), Ammonia water (25%–28% wt), Sodium borohydride (98%), Polyvinylpyrrolidone (GR), zirconium zirconium tetrachloride (98%), 2-aminoterephthalic acid (98%), and N, N-dimethylformamide (AR, $\geq 99.5\%$) were some of the synthetic raw materials used and were obtained from Sinopharm Chemical Reagent.

The crystal structure of the samples was investigated using Bruker D8 ADVANCE X-ray diffraction (XRD). External and internal morphological characteristics of the samples were explored using Hitachi SU8220 high power scanning electron microscope (SEM) and FEI Tecnai G2 F20 field emission transmission electron microscope (TEM). The chemical state of the samples was analyzed using seymerfeil 250 Xi photoelectron spectroscopy (XPS). Photocurrent-time characteristics and electronic impedance spectra (EIS) were analyzed using an electrochemical workstation (Shanghai Chenhua). UV-visible diffuse reflectance spectrum (DRS) of the samples was determined using a Daojin UV-2600 UV-vis spectrophotometer. Photoluminescence (PL) and time-resolved photoluminescence (TRPL) of the samples were determined using an FLS980 fluorescence spectrophotometer. The Bruker A 300 Electron Paramagnetic resonance (EPR) spectrometer was used to determine the active sites of the samples.

2.2 Synthesis of Flower-Like ZnO

3 mmol $\text{Zn}(\text{Ac})_2 \cdot 2\text{H}_2\text{O}$ was added to 30 mL deionized water and stirred to ensure it was evenly dissolved. Ammonia water (25%–28% wt) was then gradually added until the white precipitate was completely dissolved. Further, 48 mmol NaBH_4 was added to the solution. The mixture was stirred to ensure it was thoroughly mixed, then 0.49 g PVP was added and stirred to obtain a clear solution. The solution was transferred into a 100 mL polytetrafluoroethylene high-pressure reactor and incubated at 120°C for 3 h. After cooling to room temperature, the product was washed several times with deionized water. The resulting solid was dried at 60°C [28].

2.3 Synthesis of NU66

The hydrothermal process was used to synthesize NU66. 1 mmol zirconium tetrachloride and 1 mmol amino terephthalic acid were added to a beaker containing 50 ml DMF and stirred to ensure an even mixture. The mixture was then transferred to the polytetrafluoroethylene lining of a high-pressure reactor and incubated at 85°C for 24 h [29]. The reaction kettle was then cooled to room temperature, and the obtained solid was washed using DMF and methanol. The product was further centrifuged at 8000 r/min for 5 min and dried in a vacuum oven overnight at 60°C .

2.4 Synthesis of the NU66/ZnO Sample

NU66/ZnO samples were prepared using a simple hydrothermal *in-situ* method. The reaction conditions were the same as those used to prepare ZnO, except that 1%, 2%, 3%, 5%, and 10% were added to NU66 powder before the hydrothermal reaction.

2.5 Photocatalytic Degradation of Methylene Blue/Malachite Green

Photocatalytic performance was determined under the CEL-HXF300 xenon lamp. In the reaction, 25 mg of the sample was added into a container with 50 mL methylene blue (MB) or malachite green (MG) solution. The mixture was stirred for 1 h under dark conditions to reach the adsorption-analytical equilibrium. The mixture solution was then illuminated under a xenon lamp with a current intensity of 15 A for 1 h ($\lambda > 420$ nm). The suspension (2–3 ml) was obtained from the dispersion every 15 min. Filtering the mixture with a needle filter yielded a clear reaction solution (concentration C). The

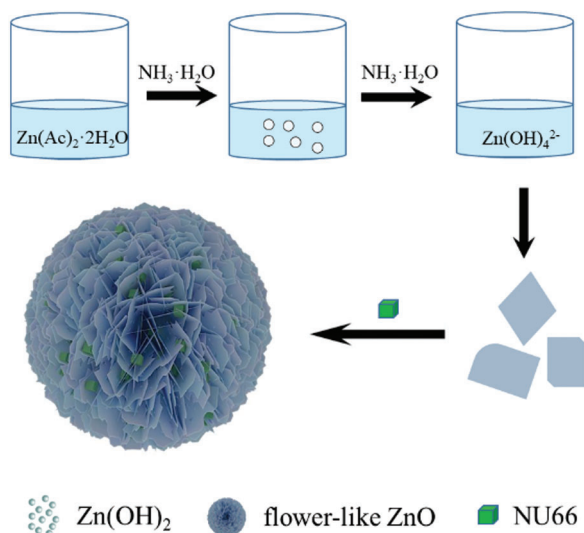
solution's absorbance was determined at 664 nm using a Shimadzu UV-2600 UV-Vis spectrophotometer. The catalyst's degradation efficiency of MB/MG solution was determined using the formula: $D = \ln(C \div C_0) \times 100\%$. According to Lambert-Beer law, the values of C_0 and C were replaced by absorption values [30,31].

2.6 Photoelectrochemical Analysis

The photoelectrochemical properties of the samples were determined with electrochemical workstation (Shanghai Chenhua) in a three electrodes cell using an electrochemical workstation (Shanghai Chenhua). A Pt plate was used as the cathode [32], Ag/AgCl electrode as the reference electrode, and FTO glass carrying catalyst was used as the working electrode. 10 mg catalyst was added to 1 ml 1% ethanol and 0.5 ml Nafion, and ultrasound was conducted for 10 min. After that, the dispersed solution was transferred to an FTO glass and dried in an XNGJ-1 infrared polymer type. Electrochemical properties were determined using a 0.2 M Na_2SO_4 solution.

3 Results and Discussion

NU66/ZnO samples were prepared using a simple hydrothermal *in-situ* method as shown in Scheme 1. $\text{Zn}(\text{OH})_2$ precipitate was formed when ammonium hydroxide was added to zinc acetate solution. To completely dissolve the $\text{Zn}(\text{OH})_2$ precipitate and form $\text{Zn}(\text{OH})_4^{2-}$, ammonia hydroxide was added. Sodium borohydride (NaBH_4) and PVP were added in that order. The as-prepared NU66 material was added before carrying out the hydrothermal reaction. The flower-like NU66/ZnO composites were formed by self-assembly through the hydrothermal reaction. The XRD diffraction peaks of ZnO (JCPDS Card No. 36-1451) at $2\theta = 31.7^\circ, 34.4^\circ, 36.2^\circ, 47.5^\circ, 62.8^\circ$ and 67.9° were identified using the crystal plane (100), (002), (101), (102), (103) and (112) of hexagonal wurtzite structure (Fig. 1) [28]. Consistency between the XRD characteristic peaks of pure ZnO and NU66/ZnO samples indicated that NU66 did not affect the formation of ZnO. However, no XRD signal was observed for NU66 in the XRD of NU66/ZnO composites. This observation can be attributed to the low NU66 content in the NU66/ZnO composite [33,34].



Scheme 1: Schematic illustration of preparation process of NU66/ZnO composite

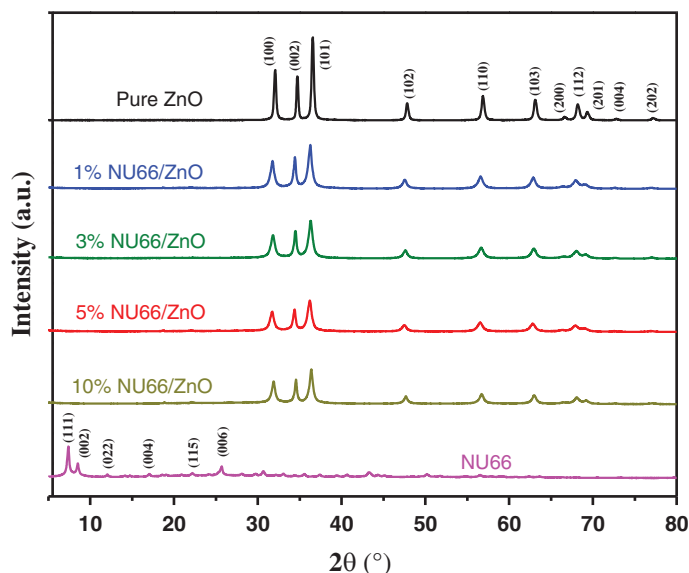


Figure 1: X-ray diffraction patterns of Pure ZnO, NU66, and NU66/ZnO composites with different doping ratios

The components and morphology of NU66/ZnO were analyzed using SEM, TEM, and element mapping (Fig. 2). The morphology of 5% NU66/ZnO was similar to that of sea urchins, and sheets in the shape of flowers were stacked on the surface (Fig. 2a). The unique shape of ZnO was attributed to the artistic synthetic process. HR-TEM image of 5% NU66/ZnO showed that the lattice spacing was 0.26 and 0.23 nm, corresponding to (101) and (110) crystal surfaces of the hexagonal wurtzite ZnO (Fig. 2b) [35]. This finding was consistent with the XRD patterns. The mapping images of 5% NU66/ZnO showed that NU66 nanoparticles were uniformly loaded in flower-like ZnO (Figs. 2c–2f), indicating the formation of a heterogeneous junction [36].

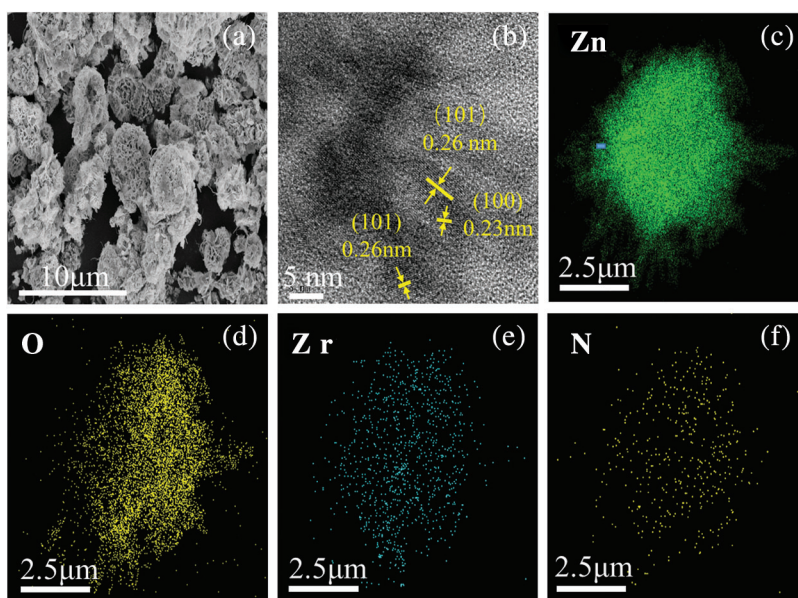


Figure 2: SEM images of (a) 5% NU66/ZnO, (b) 5% NU66/ZnO HR-TEM image, (c–f) 5% NU66/ZnO element mapping images

XPS analysis was performed to explore the chemical components and chemical states of 5% NU66/ZnO. The XPS survey spectrum of 5% NU66/ZnO revealed the presence of Zn, O, Zr, and N elements in the 5% NU66/ZnO sample, indicating that the ZnO was successfully prepared (Fig. 3a). XPS peaks located at 1044.6, 1021.5, and 499.4 eV, corresponding to Zn 2p_{3/2}, Zn 2p, and Zn LM₂ orbitals, respectively (Figs. 3b and 3c) [22]. The peak at 531.27 eV was assigned to O²⁻ ions (O 1s_{1/2}) which exists in both ZnO and NU66 (Fig. 3c). The two peaks at 185.48 and 182.98 eV were ascribed to the spin-orbit bimodal of Zr 3d_{3/2} and Zr 3d_{5/2}, respectively (Fig. 3e) [37,38]. N 1s peaks at 403.1 and 399.5 eV were assigned to Pyrrolic N and graphitic N of NU66 (Fig. 3f). XPS analysis indicated the presence of NU66 in the NU66/ZnO composite.

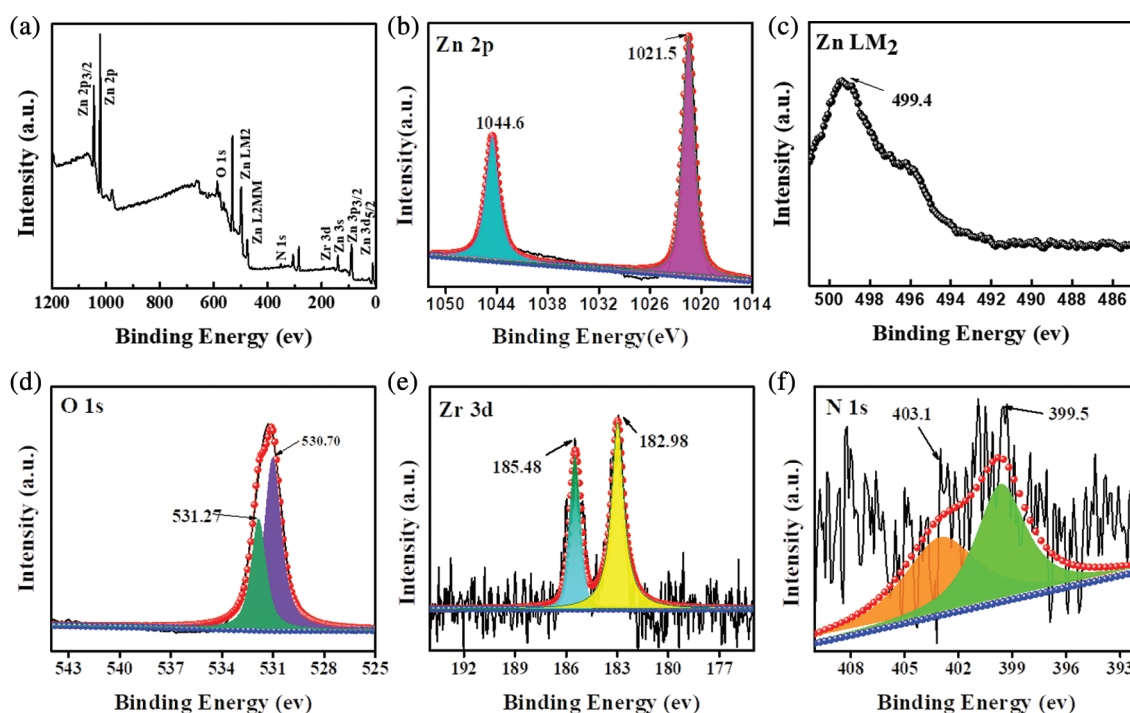


Figure 3: XPS spectra of 5% NU66/ZnO: (a) Survey, (b) Zn LM₂, (c) Zn 2p, (d) O 1s, (e) Zr 3d, and (f) N 1s

Photocatalytic evolution of NU66/ZnO composites was explored through the degradation of MB and MG. The photocatalytic activity of NU66/ZnO samples exhibited a volcanic tendency with increased NU66 content. The optimal activity of photodegradation of MB and MG was achieved with a 5% NU66/ZnO sample. These findings indicated that the ratio of NU66 in the NU66/ZnO sample can be controlled to achieve an optimal photocatalytic degradation. The photocatalytic stability of the 5% NU66/ZnO sample was determined by the cycle degradation of MB and MG (Figs. 4c and 4d). Notably, 5% NU66/ZnO sample showed stable activity without evident decay after four cycles of continuous reaction. This implied that MOF-modified ZnO samples exhibited good activity stability, indicating that they have good potential for large-scale application. Furthermore, TG curves showed good thermal stability of 5% NU66/ZnO (Fig. 5) [39]. The results of powered XRD, XPS, and SEM revealed that there were no visible structure or chemical state changes during the degradation of MB reaction (Fig. 6) [38].

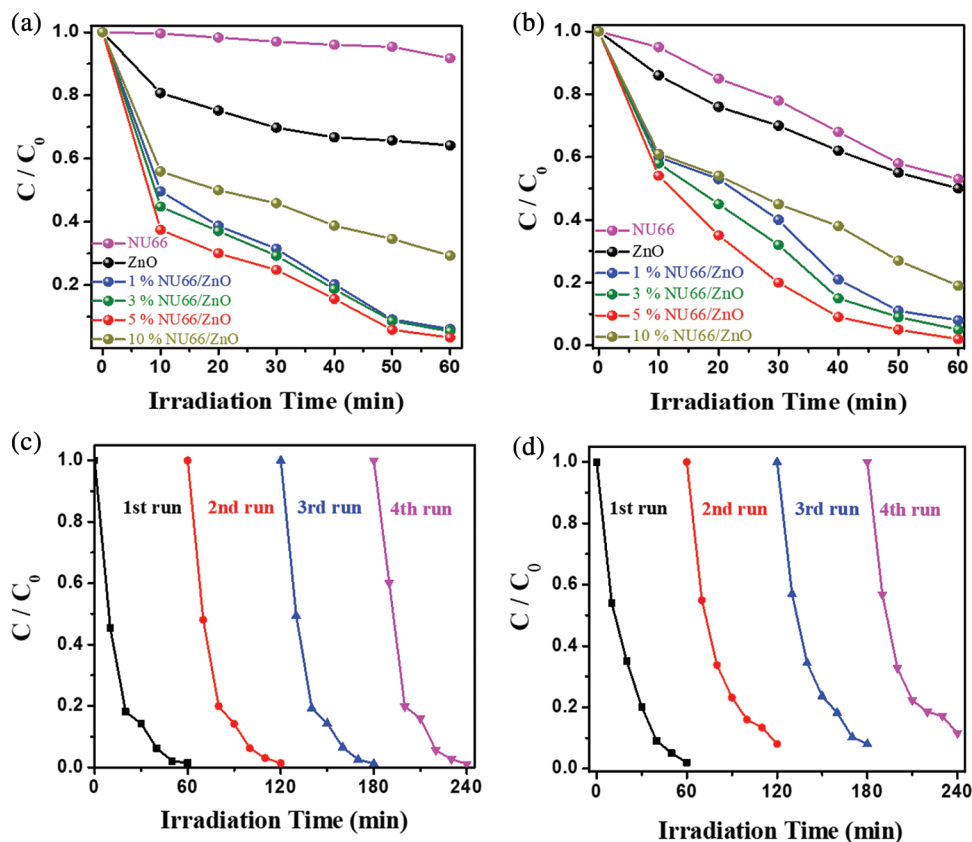


Figure 4: Photocatalytic degradation under visible light irradiation of pure ZnO, NU66 and NU66/ZnO composites (a) of MB, (b) of MG. Circulation test of 5% NU66/ZnO. (c) Photocatalytic degradation of MB. (d) Photocatalytic degradation of MG

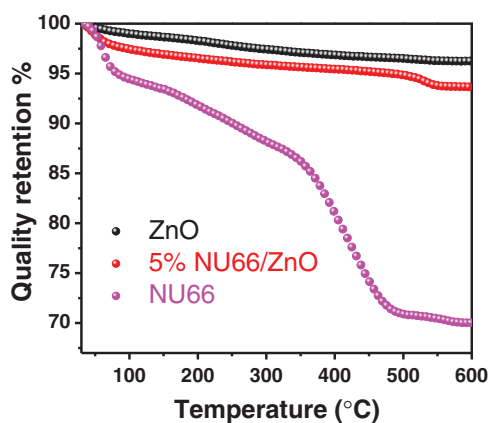


Figure 5: TG curves of ZnO, NU66, and 5% NU66/ZnO composite

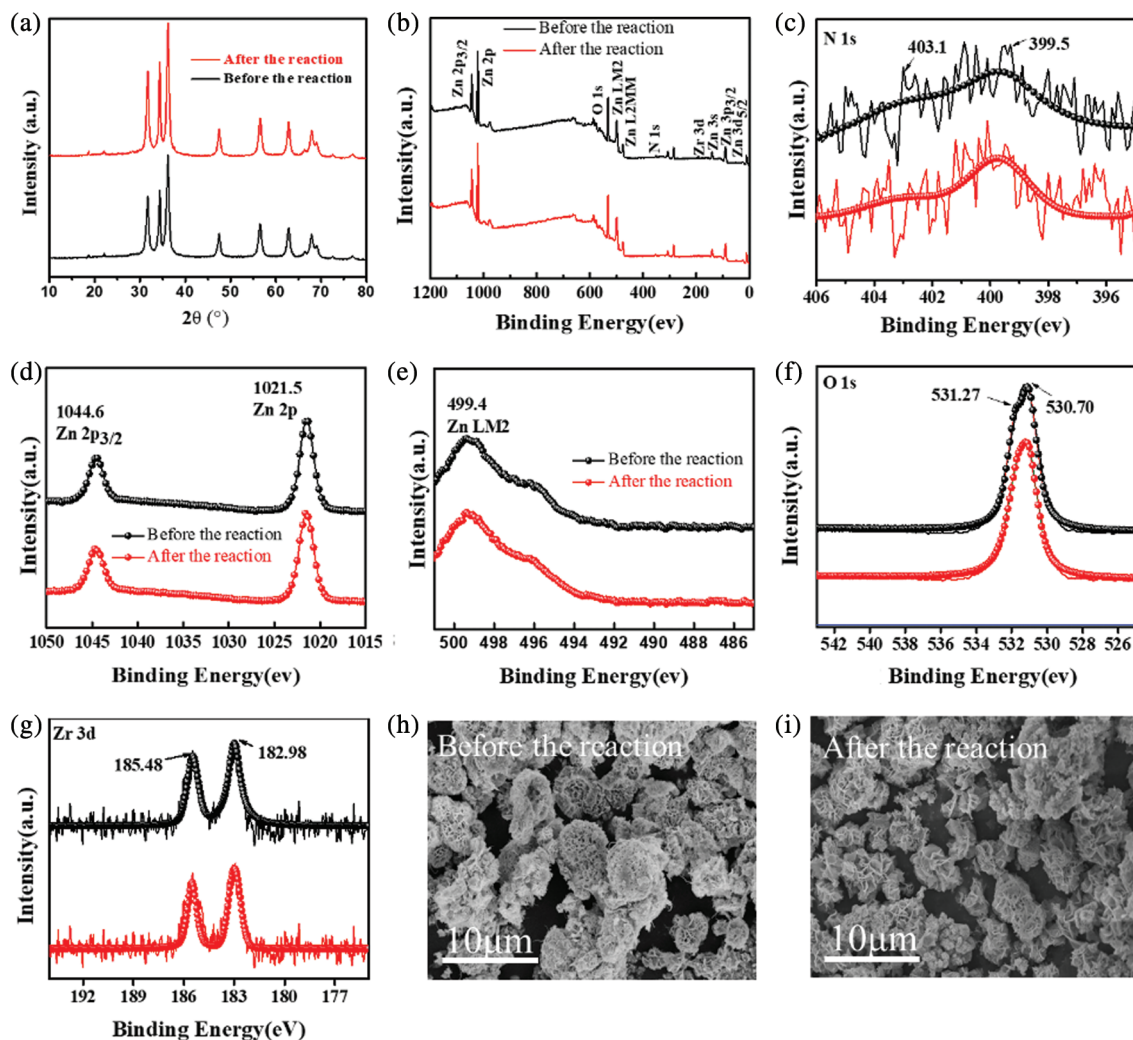
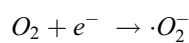
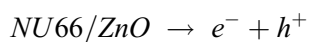


Figure 6: 5% NU66/ZnO composite before and after reaction: (a) XRD pattern, (b–g) XPS spectra, (h–i) SEM images

The main active species during photocatalytic degradation of MB were explored through the addition of three scavengers, including 1,4-benzoquinone (BQ), methyl alcohol (MeOH), and isopropyl alcohol (IPA). The addition of the scavengers in the MB system played a role in capturing superoxide radicals ($\cdot\text{O}_2^-$), hydroxyl radicals ($\cdot\text{OH}$), and holes (h^+). The efficiency of photocatalytic degradation decreased significantly as the amount of BQ increased, whereas the addition of MeOH and IPA had no significant effect on photocatalytic degradation (Fig. 7a). This result reveals that the primary active species in the degradation process was $\cdot\text{O}_2^-$. The EPR results were consistent with the observation that $\cdot\text{O}_2^-$ was the main active species in the system (Figs. 7b–7d) [40]. The possible degradation mechanism of MB/MG is presented below:



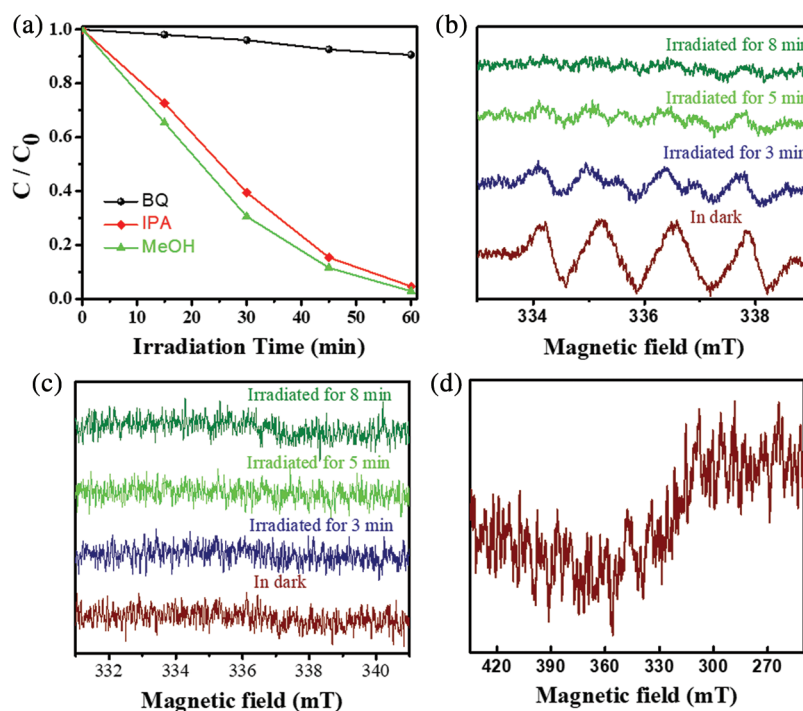


Figure 7: (a) Effect of different scavengers on the degradation of MB in 5% NU66/ZnO composite under visible light irradiation, ESR spectra of 5% NU66/ZnO under illumination conditions for detection of (b) $\bullet\text{O}_2^-$ radicals, (c) $\bullet\text{OH}$ radicals, (d) h^+ ions

To elucidate the mechanisms underlying the enhanced photoactivity, optical and photoelectrical properties of the NU66/ZnO composite were investigated. With increasing NU66 content in the NU66/ZnO composite, a redshift in the DRS curve was observed (Fig. 8a). The bandgap of ZnO and 5% NU66/ZnO narrowed from 3.00 to 2.86 eV. The conduction band (CB) positions of NU66 and ZnO were measured using Mott-Schottky curves, which were -0.6 and -0.4 eV, respectively. Thus, NU66 and ZnO had valent bands of 2.6 and 1.7 eV, respectively. Because the conduction band bottom of the NU66 was higher than that of ZnO, the electrons in the ZnO conduction band could not be transmitted to the conduction band of NU66. Thus, the only area for a large number of ZnO electrons to migrate from the conduction band to the valence band of the NU66. This is a typical Z-scheme photocatalysts mechanism [41]. Increased photocatalytic activity in visible-light irradiation can be attributed to broadening light absorption. Photoluminescence (PL) spectra and time-resolved PL spectra were analyzed to explore the charge-carrier behavior of the products [42]. The fluorescence intensity of 5% UN66/ZnO was significantly quenched relative to that of pure ZnO (Fig. 8c), indicating that the charge recombination was suppressed in 5% UN66/ZnO composite. The average lifetime of 5% NU66/ZnO composite was (125 ns) lower compared to that of ZnO (177 ns) owing to the rapid transfer of photoelectrons between NU66 and ZnO (Fig. 8d) [43]. The charge separation condition was further explored through transient photocurrent and electrochemical impedance spectroscopy (EIS) [44]. A significant increase in photocurrent and decrease in impedance was observed in 5% UN66/ZnO composite (Figs. 8e and 8f). This implied that the

separation efficiency and conductivity of optical charge carriers of 5% NU66/ZnO were much better compared with that of pure ZnO. Additionally, the enhanced photocatalytic activity can be attributed to optimized photoelectric properties [45,46]. According to above experimental data, the possible mechanism of degradation of MB/MG is speculated as follows: As shown in Scheme 2, Type II mechanism of charge transfer route in the NU66/ZnO composites was proposed. Under the visible light irradiation, photo-generated electron (e^-) transferring from the conduction band (CB) of UN66 to CB of ZnO, and photogenerated hole (h^+) transferring from the valence band (VB) of ZnO to h^+ of UN66. Thus, Type II heterojunction was formed. Subsequently, O_2 in environment reacted with e^- to form O_2^- in the conduction band of NU66. Then, the active species O_2^- attack the MB/MG pollutants to product CO_2 and H_2O , achieving the remarkably enhanced photodegradation of MB/MG pollutants.

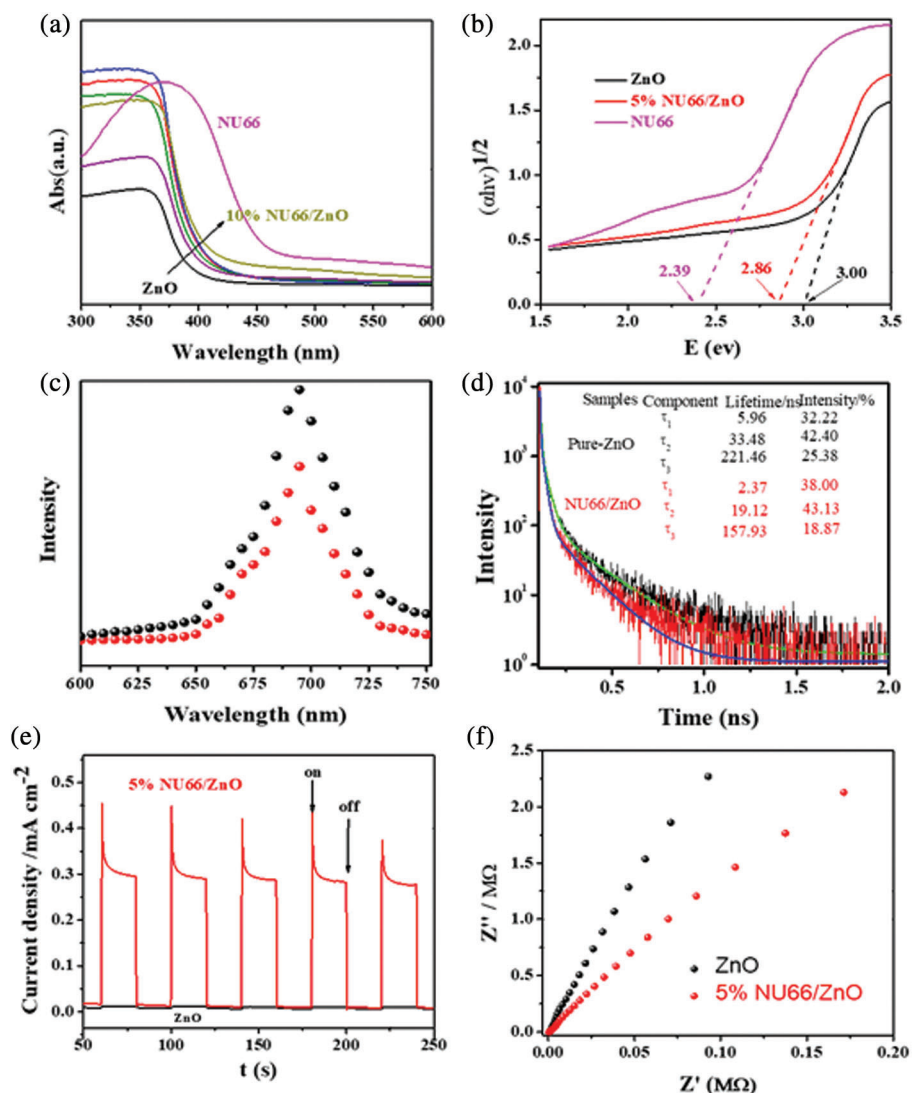
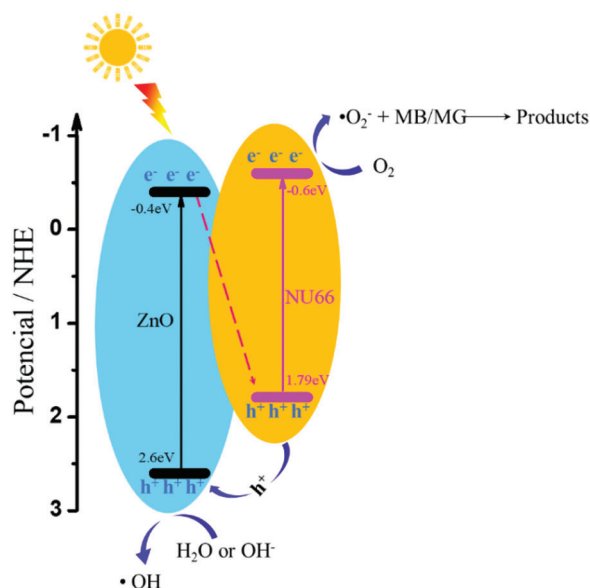


Figure 8: (a) UV-Vis DRS of pure ZnO, NU66 and NU66/ZnO photocatalysts, (b) bandgap of pure ZnO, NU66 and 5% NU66/ZnO composite, (c) PL spectra, (d) Time-resolved PL spectra, (e) Photocurrent properties, (f) Nyquist diagram showing electrochemical impedance of pure ZnO and 5% NU66/ZnO composite



Scheme 2: Mechanism of photodegradation of MB/MG by NU66/ZnO photocatalysts

4 Conclusion

In this study, a novel flower-like hierarchically NU66/ZnO composite was prepared for dye removal via *in situ* hydrothermal synthetic routes. The resulting NU66/ZnO composites had a significantly larger specific area and micropore volume than prepared samples of ZnO and NU66 and also exhibited significantly higher removal efficiency for MB (96.7% after 1 h) and MG (98% after 1 h) when compared to pure NU66 nanoparticles. The loading of $\text{NH}_2\text{-UiO-66}$ into the NU66/ZnO nanoparticles provided more accessible entry points for the uptake of MB and MG. This improved the interaction between catalysts and dyes hence improving photocatalytic performance. The EPR results demonstrated that $\bullet\text{O}_2^-$ was the main active species in the degradation process. The NU66/ZnO composites' superior dye removal performance was attributed to their enhanced adsorption properties, more active sites, and improved efficiency of charge separation under visible-light irradiation photocatalyzed reaction. Due to their high thermal stability, structural stability, and catalytic activity, the NU66/ZnO heterojunctions have a high potential for industrial applications, where they owing to the good thermal stability, structural stability and high catalytic activity, which may replace conventional photocatalysts in the removal of organic contaminants.

Acknowledgement: This work was financially supported by the Zhoushan Science and Technology Project (2020C21023), Zhoushan Free Trade Zone International Cooperation (2019010301), Putu District of Zhoushan Environmental Special Supporting Project (PT2020e001). Authors thank Shiyanjia Lab and Ceshigo testing institutions for technical support.

Funding Statement: This work was financially supported by the Zhoushan Science and Technology Project (2020C21023), Zhoushan Free Trade Zone International Cooperation (2019010301), Putu District of Zhoushan Environmental Special Supporting Project (PT2020e001).

Conflicts of Interest: The authors declare that they have no conflicts of interest to report regarding the present study.

References

1. Kiriarachchi, H. D., Abouzeid, K. M., Bo, L., El-Shall, M. S. (2019). Growth mechanism of sea urchin ZnO nanostructures in aqueous solutions and their photocatalytic activity for the degradation of organic dyes. *ACS Omega*, 4(9), 14013–14020. DOI 10.1021/acsomega.9b01772.
2. Zou, Z., Ye, J., Sayama, K., Arakawa, H. (2001). Direct splitting of water under visible light irradiation with an oxide semiconductor photocatalyst. *Nature*, 414, 625–727. DOI 10.1038/414625a.
3. Nie, N., Zhang, L., Fu, J., Cheng, B., Yu, J. (2018). Self-assembled hierarchical direct Z-scheme g-C₃N₄/ZnO microspheres with enhanced photocatalytic CO₂ reduction performance. *Applied Surface Science*, 441, 12–22. DOI 10.1016/j.apsusc.2018.01.193.
4. Wang, X., Maeda, K., Thomas, A., Takanabe, K., Xin, G. et al. (2009). A metal-free polymeric photocatalyst for hydrogen production from water under visible light. *Nature Materials*, 8, 76–80. DOI 10.1038/nmat2317.
5. Mimouni, R., Askri, B., Larbi, T., Amlouk, M., Meftah, A. (2020). Photocatalytic degradation and photo-generated hydrophilicity of methylene blue over ZnO/ZnCr₂O₄ nanocomposite under stimulated UV light irradiation. *Inorganic Chemistry Communications*, 115, 107889. DOI 10.1016/j.inoche.2020.107889.
6. Lin, J., Luo, Z., Liu, J., Li, P. (2018). Photocatalytic degradation of methylene blue in aqueous solution by using ZnO-SnO₂ nanocomposites. *Materials Science in Semiconductor Processing*, 87, 24–31. DOI 10.1016/j.mssp.2018.07.003.
7. Sukriti, Chand, P., Singh, V., Kumar, D. (2020). Rapid visible light-driven photocatalytic degradation using Ce-doped ZnO nanocatalysts. *Vacuum*, 178, 109364. DOI 10.1016/j.vacuum.2020.109364.
8. Mahmud, R. A., Shafawi, A. N., Ahmed Ali, K., Putri, L. K., Md Rosli, N. I. et al. (2020). Graphene nanoplatelets with low defect density as a synergetic adsorbent and electron sink for ZnO in the photocatalytic degradation of methylene blue under UV-vis irradiation. *Materials Research Bulletin*, 128, 110876. DOI 10.1016/j.materresbull.2020.110876.
9. Sha, Z., Wu, J. (2015). Enhanced visible-light photocatalytic performance of BiOBr/Uio-66(Zr) composite for dye degradation with the assistance of Uio-66. *RSC Advances*, 49, 39592–39600. DOI 10.1039/c5ra04869a.
10. Sha, Z., Sun, J., Chan, H. S. O., Jaenicke, S., Wu, J. (2015). Enhanced photocatalytic activity of the AgI/Uio-66 (Zr) composite for rhodamine B degradation under visible-light irradiation. *Chempluschem*, 80(8), 1321–1328. DOI 10.1002/cplu.201402430.
11. Arsalani, N., Bazazi, S., Abuali, M., Jodeyri, S. (2020). A new method for preparing ZnO/CNT nanocomposites with enhanced photocatalytic degradation of malachite green under visible light. *Journal of Photochemistry and Photobiology A: Chemistry*, 389, 1122207. DOI 10.1016/j.jphotochem.2019.112207.
12. Gang, R., Xu, L., Xia, Y., Cai, J., Zhang, L. et al. (2020). Fabrication of MoS₂ QDs/ZnO nanosheet 0D/2D heterojunction photocatalysts for organic dyes and gaseous heavy metal removal. *Journal of Colloid and Interface Science*, 579, 853–861. DOI 10.1016/j.jcis.2020.06.116.
13. Adeleke, J. T., Theivasanthi, T., Thirupathi, M., Swaminathan, M., Akomolafe, T. et al. (2018). Photocatalytic degradation of methylene blue by ZnO/NiFe₂O₄ nanoparticles. *Applied Surface Science*, 455, 195–200. DOI 10.1016/j.apsusc.2018.05.184.
14. Wang, M., Ye, M., Iocozzia, J., Lin, C., Lin, Z. (2016). Plasmon-mediated solar energy conversion via photocatalysis in noble metal/Semiconductor composites. *Advanced Science*, 3(6), 1600024. DOI 10.1002/adv.201600024.
15. Zang, S., Zhang, G., Lan, Z. A., Zheng, D., Wang, X. (2019). Enhancement of photocatalytic H₂ evolution on pyrene-based polymer promoted by MoS₂ and visible light. *Applied Catalysis B: Environmental*, 251, 102–111. DOI 10.1016/j.apcatb.2019.03.061.
16. Kwon, D., Kim, J. (2020). Silver-doped ZnO for photocatalytic degradation of methylene blue. *Korean Journal of Chemical Engineering*, 37, 1226–1232. DOI 10.1007/s11814-020-0520-7.
17. Demille, T. B., Hughes, R. A., Preston, A. S., Adelung, R., Mishra, Y. K. et al. (2018). Light-mediated growth of noble metal nanostructures (Au, Ag, Cu, Pt, Pd, Ru, Ir, Rh) from micro- and nanoscale ZnO tetrapodal backbones. *Frontiers in Chemistry*, 6, 411. DOI 10.3389/fchem.2018.00411.

18. Lu, J., Liu, M., Zhou, S., Zhou, X., Yang, Y. (2017). Electrospinning fabrication of ZnWO₄ nanofibers and photocatalytic performance for organic dyes. *Dyes and Pigments*, 136, 1–7. DOI 10.1016/j.dyepig.2016.08.008.
19. Madhusudan, P., Wang, Y., Chandrashekar, B. N., Wang, W., Wang, J. et al. (2019). Nature inspired ZnO/ZnS nanobranch-like composites, decorated with Cu(OH)₂ clusters for enhanced visible-light photocatalytic hydrogen evolution. *Applied Catalysis B: Environmental*, 253, 379–390. DOI 10.1016/j.apcatb.2019.04.008.
20. Baeissa, E. S. (2016). Environmental remediation of Cr(VI) solutions using Ni-bismuth oxyiodide nanospheres. *Desalination and Water Treatment*, 57(59), 28939–28946. DOI 10.1080/19443994.2016.1195291.
21. Li, Z., Li, C., Ge, X., Ma, J., Zhang, Z. et al. (2016). Reduced graphene oxide wrapped MOFs-derived cobalt-doped porous carbon polyhedrons as sulfur immobilizers as cathodes for high performance lithium sulfur batteries. *Nano Energy*, 23, 15–26. DOI 10.1016/j.nanoen.2016.02.049.
22. Cheng, C., Fang, J., Lu, S., Cen, C., Chen, Y. et al. (2016). Zirconium metal-organic framework supported highly-dispersed nanosized BiVO₄ for enhanced visible-light photocatalytic applications. *Journal of Chemical Technology & Biotechnology*, 91(11), 2785–2792. DOI 10.1002/jctb.4885.
23. Du, X. D., Yi, X. H., Wang, P., Zheng, W., Deng, J. et al. (2019). Robust photocatalytic reduction of Cr(VI) on UiO-66-NH₂(Zr/Hf) metal-organic framework membrane under sunlight irradiation. *Chemical Engineering Journal*, 356, 393–399. DOI 10.1016/j.cej.2018.09.084.
24. Zhang, Z., Wang, S., Bao, M., Ren, J., Pei, S. et al. (2019). Construction of ternary Ag/AgCl/NH₂-UiO-66 hybridized heterojunction for effective photocatalytic hexavalent chromium reduction. *Journal of Colloid and Interface Science*, 555, 342–351. DOI 10.1016/j.jcis.2019.07.103.
25. Sha, Z., Chan, H. S., Wu, J. (2015). Ag₂CO₃/UiO-66(Zr) composite with enhanced visible-light promoted photocatalytic activity for dye degradation. *Journal of Hazardous Materials*, 299, 132–140. DOI 10.1016/j.jhazmat.2015.06.016.
26. Zhao, C., Zhang, Y., Jiang, H., Chen, J., Liu, Y. et al. (2019). Combined effects of octahedron NH₂-UiO-66 and flowerlike ZnIn₂S₄ microspheres for photocatalytic dye degradation and hydrogen evolution under visible light. *The Journal of Physical Chemistry C*, 123(29), 18037–18049. DOI 10.1021/acs.jpcc.9b03807.
27. Liang, Q., Zhang, C., Xu, S., Zhou, M., Zhou, Y. et al. (2020). *In situ* growth of CdS quantum dots on phosphorus-doped carbon nitride hollow tubes as active 0D/1D heterostructures for photocatalytic hydrogen evolution. *Journal of Colloid and Interface Science*, 577, 1–11. DOI 10.1016/j.jcis.2020.05.053.
28. Yuan, Y. P., Yin, L. S., Cao, S. W., Xu, G. S., Li, C. H. et al. (2015). Improving photocatalytic hydrogen production of metal-organic framework UiO-66 octahedrons by dye-sensitization. *Applied Catalysis B: Environmental*, 168–169, 572–576. DOI 10.1016/j.apcatb.2014.11.007.
29. Lei, C., Pi, M., Jiang, C., Cheng, B., Yu, J. (2017). Synthesis of hierarchical porous zinc oxide (ZnO) microspheres with highly efficient adsorption of Congo red. *Journal of Colloid and Interface Science*, 490, 242–251. DOI 10.1016/j.jcis.2016.11.049.
30. Jin, J., Liang, Q., Ding, C., Li, Z., Xu, S. (2017). Simultaneous synthesis-immobilization of Ag nanoparticles functionalized 2D g-C₃N₄ nanosheets with improved photocatalytic activity. *Journal of Alloys and Compounds*, 691, 763–771. DOI 10.1016/j.jallcom.2016.08.302.
31. Lee, D. T., Zhao, J., Oldham, C. J., Peterson, G. W., Parsons, G. N. (2017). UiO-66-NH₂ metal-organic framework (MOF) nucleation on TiO₂, ZnO, and Al₂O₃ atomic layer deposition-treated polymer fibers: Role of metal oxide on MOF growth and catalytic hydrolysis of chemical warfare agent simulants. *ACS Applied Materials & Interfaces*, 9(51), 44847–44855. DOI 10.1021/acsami.7b15397.
32. Zhang, S. C., Liu, Z. F., Ruan, M. N., Guo, Z. G. (2020). Enhanced piezoelectric-effect-assisted photoelectrochemical performance in ZnO modified with dual cocatalysts. *Applied Catalysis B: Environmental*, 262, 118279. DOI 10.1016/j.apcatb.2019.118279.
33. Zhou, Y., Yang, L., Lu, J., Wu, Y., Li, C. et al. (2016). Photoelectric properties of three-dimensional urchin-like zinc oxide/titanium dioxide composite micro nanostructures. *Micro & Nano Letters*, 11(5), 277–280. DOI 10.1049/mnl.2015.0394.

34. Zhang, G., Lin, L., Li, G., Zhang, Y., Savateev, A. et al. (2018). Ionothermal synthesis of triazine-heptazine-based copolymers with apparent quantum yields of 60% at 420 nm for solar hydrogen production from “Sea water”. *Angewandte Chemie International Edition English*, 57(30), 9372–9376. DOI 10.1002/anie.201804702.
35. Chen, Q., He, Q., Lv, M., Xu, Y., Yang, H. et al. (2015). Selective adsorption of cationic dyes by UiO-66-NH₂. *Applied Surface Science*, 327, 77–85. DOI 10.1016/j.apsusc.2014.11.103.
36. Sun, L., Shao, Q., Zhang, Y., Jiang, H., Ge, S. et al. (2020). N self-doped ZnO derived from microwave hydrothermal synthesized zeolitic imidazolate framework-8 toward enhanced photocatalytic degradation of methylene blue. *Journal of Colloid and Interface Science*, 565, 142–155. DOI 10.1016/j.jcis.2019.12.107.
37. Abdel-wahab, M. S., Jilani, A., Yahia, I. S., Al-Ghamdi, A. A. (2016). Enhanced the photocatalytic activity of Ni-doped ZnO thin films: Morphological, optical and XPS analysis. *Superlattices and Microstructures*, 94, 108–118. DOI 10.1016/j.spmi.2016.03.043.
38. Lin, S., Zhang, Y., You, Y., Zeng, C., Xiao, X. et al. (2019). Bifunctional hydrogen production and storage on 0D–1D heterojunction of Cd_{0.5}Zn_{0.5}S@Halloysites. *Advanced Functional Materials*, 29(39), 1903825. DOI 10.1002/adfm.201903825.
39. Yu, Z. J., Kumar, M. R., Sun, D. L., Wang, L. T., Hong, R. Y. (2016). Large scale production of hexagonal ZnO nanoparticles using PVP as a surfactant. *Materials Letters*, 166, 284–287. DOI 10.1016/j.matlet.2015.12.102.
40. Molavi, H., Eskandari, A., Shojaei, A., Mousavi, S. A. (2018). Enhancing CO₂/N₂ adsorption selectivity via post-synthetic modification of NH₂-UiO-66(Zr). *Microporous and Mesoporous Materials*, 257, 193–201. DOI 10.1016/j.micromeso.2017.08.043.
41. Han, L., Jing, F., Zhang, J., Luo, X. Z., Zhong, Y. L. et al. (2021). Environment friendly and remarkably efficient photocatalytic hydrogen evolution based on metal organic framework derived hexagonal/cubic In₂O₃ phase-junction. *Applied Catalysis B: Environmental*, 282, 119602. DOI 10.1016/j.apcatb.2020.119602.
42. Yang, W., Zhang, L., Xie, J., Zhang, X., Liu, Q. et al. (2016). Enhanced photoexcited carrier separation in oxygen-doped ZnIn₂S₄ nanosheets for hydrogen evolution. *Angewandte Chemie International Edition English*, 55(23), 6716–20. DOI 10.1002/anie.201602543.
43. Zang, S., Zhang, G., Yang, P., Zheng, D., Wang, X. (2019). Polymeric donor-acceptor heterostructures for enhanced photocatalytic H₂ evolution without using Pt cocatalysts. *Chemistry*, 25(24), 6102–6107. DOI 10.1002/chem.201900414.
44. Liang, Z., Bai, X., Hao, P., Guo, Y., Xue, Y. et al. (2019). Full solar spectrum photocatalytic oxygen evolution by carbon-coated TiO₂ hierarchical nanotubes. *Applied Catalysis B: Environmental*, 243, 711–720. DOI 10.1016/j.apcatb.2018.11.017.
45. Liu, Y., Wang, R., Yang, Z., Du, H., Jiang, Y. et al. (2015). Enhanced visible-light photocatalytic activity of Z-scheme graphitic carbon nitride/oxygen vacancy-rich zinc oxide hybrid photocatalysts. *Chinese Journal of Catalysis*, 36(12), 2135–2144. DOI 10.1016/s1872-2067(15)60985-8.
46. Kumar, A., Sharma, G., Kumari, A., Guo, C., Naushad, M. et al. (2021). Construction of dual Z-scheme g-C₃N₄/Bi₄Ti₃O₁₂/Bi₄O₅I₂ heterojunction for visible and solar powered coupled photocatalytic antibiotic degradation and hydrogen production: Boosting via Γ/I_3^- and Bi³⁺/Bi⁵⁺ redox mediators. *Applied Catalysis B: Environmental*, 284, 119808. DOI 10.1016/j.apcatb.2020.119808.